Inertial Torsion Noise in Matter-Wave Interferometers for Gravity Experiments

Meng-Zhi Wu,[1, *] Marko Toroš,[2, 3] Sougato Bose,[2] and Anupam Mazumdar[1, †]

[1] Van Swinderen Institute for Particle Physics and Gravity,
University of Groningen, 9747 AG Groningen, the Netherlands
[2] Department of Physics and Astronomy, University College London, Gower Street, WC1E 6BT London, UK
[3] Faculty of Mathematics and Physics, University of Ljubljana, Jadranska 19, SI-1000 Ljubljana, Slovenia

Matter-wave interferometry is susceptible to non-inertial noise sources, which can induce dephasing and a resulting loss of interferometric visibility. Here, we focus on inertial torsion noise (ITN), which arises from the rotational motion of the experimental apparatus suspended by a thin wire and subject to random external torques. We provide analytical expressions for the ITN noise starting from generalized Langevin equations describing the experimental box which can then be used together with the transfer function to obtain the dephasing factor. We verify the theoretical modelling and the validity of the approximations using Monte Carlo simulations, obtaining good agreement between theory and numerics. As an application, we estimate the size of the effects for the next generation of interferometry experiments with femtogram particles, which could be used as the building block for entanglement-based tests of the quantum nature of gravity. We find that the ambient gas is a weak source of ITN, posing mild restrictions on the ambient pressure and temperature. We discuss the general ITN constraints by assuming a Langevin equation parameterized by three phenomenological parameters.

I. INTRODUCTION

Matter-wave interferometry has many salient applications for gravitational physics with devices spanning gravimeters [1], gradiometers [2, 3], accelerometers [4] and gyroscopes [5]. They can also be used for fundamental physics, such as testing the equivalence principle [6–8] and the quantum gravity induced entangled of masses (QGEM) to test the quantum nature of gravity in a lab [9, 10], see also [11–14]. The paper [14] provides the protocol to test the spin-2 nature of the graviton in an analogue of the light-bending experiment, see also [13]. One can also probe the nature of massive graviton [15] and non-local gravitational interaction [16] motivated by string theory. Furthermore, some groups even consider building gravitational wave observatories based on matter-wave interferometry such as the matter-wave laser interferometer gravitation antenna (MIGA) [17, 18], the matter-wave atomic gradiometer interferometric sensor (MAGIS-100) [19, 20], as well as the mesoscopic interference for metric and curvature (MIMAC) scheme [21].

Future matter-wave interferometry aims to exploit the regime of large masses, large superposition sizes, and long coherence times, allowing the probe of exquisitely small experimental signals. For example, the QGEM experiment would ideally require a test mass of $\sim 10^{-15}$ kg, a superposition size of $\sim 100\,\mu$m, and a coherence time of ~ 1 s [8, 9, 22–24]. One of the most promising setups towards this kind of experiments is the adaptation of the Stern-Gerlach interferometer (SGI) to nanoparticles [25]. SGIs based on atom chips [26] have already achieved the superposition size and coherence time of $3.93\,\mu$m and

21.45 ms for the half-loop configuration [27], respectively, and $0.38\,\mu$m and 7 ms for the full-loop configuration [28], respectively. The next generation of SGIs is currently under theoretical and numerical investigation [29–33].

An essential challenge of matter-wave interferometry is to tame the numerous noise sources, which can cause random phase fluctuations, resulting in dephasing and the loss of interferometric visibility. Vibrations of the experiment apparatus can result in residual acceleration noise (RAN) [34, 35], external sources of gravity can induce gradient gradient noise (GGN) [18, 20, 35, 36], and charged or dipolar environmental particles can induce several electromagnetic channels of dephasing [37, 38], besides gravitational decoherence [39] of the QGEM.

This paper will study the dephasing caused by the residual rotational or inertial torsion noise (ITN) for an asymmetric nanoparticle matter-wave interferometer which is sensitive to gravity-gradients [21, 35, 36]. ITN arises naturally in any setup whenever the experimental apparatus is subject to random torques, placing it in non-inertial rotational motion. As we will see, ITN can induce relative random phases in an interferometric experiment, resulting in a loss of interferometric contrast. Here, we will be primarily interested in understanding ITN, and we will focus on a simple single-stage suspension forming a torsion pendulum, i.e., matter-wave interferometry performed inside a hanging box. Analogous configurations of the experimental apparatus have been investigated previously in gravitational wave observatories like LIGO [40] and VIRGO [41]. More advanced setups could employ additional structures like the inverted pendulum [42] and the Roberts linkage [43].

In Sec. II, we first introduce the concept of ITN, illustrating it for matter-wave interferometry that can be modelled using qubits. In Sec. III, we generalize the analysis using linear response theory, providing the transfer function and its relation to the dephasing factor. In

* mengzhi.wu@rug.nl
† anupam.mazumdar@rug.nl

Sec. IV, we investigate ITN caused by ambient gas collisions on the experimental box starting from a generalized classical Langevin equation. We will compute the power spectrum density (PSD) of the ITN using the convolution theorem and verify the validity of the approximations using Monte Carlo simulations. In Sec. V, we obtain the resulting constraints on the ambient pressure and temperature and general constraints on ITN by parametrizing a generic Langevin equation modelling the experimental box with three phenomenological parameters in the dynamical equation of the experimental box. In Sec. VI, we conclude with a summary of the obtained results. In Appendix A, we construct the ITN Lagrangian starting from Fermi normal coordinates and transforming to a rotating reference frame. In Appendix B, we provide for completeness and also the complete derivation of the ITN PSD using complex analysis. In Appendix C, we analyze the ITN caused by the ambient thermal gas collision.

II. CONCEPT OF INERTIAL TORSION NOISE AND DEPHASING

Suppose the interferometer is set up in a suspended experiment apparatus, shown as Fig. 1(a). A natural reference frame is the comoving frame of the experimental apparatus. For instance, consider a Stern-Gerlach interferometer controlled by a static magnetic field $\mathbf{B}(x, y, z)$, which holds for the comoving frame of the experiment apparatus. If the SGI is studied under another reference frame which moves relative to the comoving reference, then the Lorentzian transformation of the magnetic field $\mathbf{B}(t)$ has to be taken into account, and even the induced electric field also needs to be studied. The comoving reference frame of the experiment apparatus is thus preferred as it simplifies the analysis.

However, the experimental apparatus itself can also be shaken by various environmental disturbances, such as vibrations of mechanical supports and jitter caused by collisions of air molecules. These vibrations of the experimental apparatus are applied to the interferometer as non-inertial forces, resulting in acceleration and rotation noises, affecting the interferometer's final phase, i.e., *residual acceleration noise* (RAN) [35, 36] and *inertial rotation noise* (ITN) which we investigate in this paper. Such noises can induce dephasing, which can be mitigated only by carefully controlling the experimental setup and its environment.

In this paper, we will focus on the Stern-Gerlach interferometer with the configuration shown in Fig. 1(b), which can be achieved by a system with a spin-1 state and spin-0 state (embedded in an object) in a magnetic field with a constant gradient, see [21]. In particular, the system is prepared in a spin superposition of $|S = 0\rangle$ and $|S = 1\rangle$, say $|\psi\rangle = 1/\sqrt{2}(|S = 0\rangle + |S = 1\rangle)$. At the same time, the external magnetic field has a linear spatial distribution in the x-axis, i.e. $B(x) = B_0 + \eta x$, where the magnetic gradient η will flip several times to accelerate

and decelerate the state $|S = 1\rangle$.

Therefore, the acceleration of the $|S = 1\rangle$ state is a constant $a_m = g\mu_B\eta$ during $0 \sim t_a$ and $3t_a + t_e \sim 4t_a + t_e$, and $a_m = -g\mu_B\eta$ during $t_a \sim 2t_a$ and $2t_a + t_e \sim 3t_a + t_e$, where $g = 2$ is the Lande factor and $\mu_B = 9.27 \times 10^{-24}$ J/T is the Bohr magneton.

In an ideal experiment (without any dephasing and decoherence), the final state of the system is

$$|\psi\rangle = \frac{1}{\sqrt{2}}e^{i\phi_{\text{global}}}(|S = 0, L\rangle + e^{i\phi_{\text{diff}}}|S = 1, R\rangle), \quad (1)$$

where ϕ_{global} is the global phase of the quantum state and ϕ_{diff} is the differential phase between two paths denoted as "L" and "R". The global phase does not have observable effects, while the differential phase ϕ_{diff} usually encodes the signal we want to extract. For example, ϕ_{diff} is related to the gravitation acceleration g for a gravimeter [44]. Another example is the QGEM experiment, which encodes information about the nature of gravity.

However, some classical noises like RAN and ITN always exist. They will contribute some random phase $\delta\phi$ on ϕ_{diff}. Although $e^{i\delta\phi}$ itself is a pure phase, the ensemble average of such a random phase can lead to a damping factor, known as a dephasing effect. For ease of convenience, $\delta\phi$ is supposed to follow a Gaussian distribution with a mean value of zero and a variance of $\Gamma \equiv \mathbb{E}[(\delta\phi)^2]/2$, then the expectation value of the phase can be computed as

$$\mathbb{E}[e^{i\delta\phi}] = e^{-\mathbb{E}[(\delta\phi)^2]} \equiv e^{-\Gamma}, \quad (2)$$

where $\mathbb{E}[\cdot]$ is the ensemble average of random variables. Note that for a more general probability distribution of $\delta\phi$, one can also define a similar Γ to describe the dephasing effect [45]. Such decay factor $e^{-\Gamma}$ will cause the loss of visibility of the interferometer. In particular, consider the ensemble average of the density matrix $\hat{\rho} = |\psi\rangle \langle \psi|$:

$$\mathbb{E}[\hat{\rho}] = \frac{1}{2}\bigg(|L\rangle \langle L| + |R\rangle \langle R|$$
$$+ \mathbb{E}[e^{i\delta\phi}]e^{2i\phi_{\text{diff}}}|R\rangle \langle L| + \mathbb{E}[e^{-i\delta\phi}]e^{-2i\phi_{\text{diff}}}|L\rangle \langle R|\bigg), \quad (3)$$

the off-diagonal terms decay exponentially with the damping given by the variance Γ. Consequently, the expectation value $\text{Tr}(\hat{W}\hat{\rho})$ of any witness operator $\hat{W}$ will also decay with respect to the factor $e^{-\Gamma}$.

For example, one can consider two applications of matter-wave interferometers for gravity experiments.

- The first application is the gravimeter based on a NV center [44, 46]. The gravitational acceleration g is proportional to the differential phase as $\phi_{\text{diff}} = 16\pi mg\Delta z/(\hbar\omega_0)$, where Δz is the superposition size along the z-axis, and $\omega_0 \sim 100$ kHz is the trapping frequency. Then the phase fluctuation
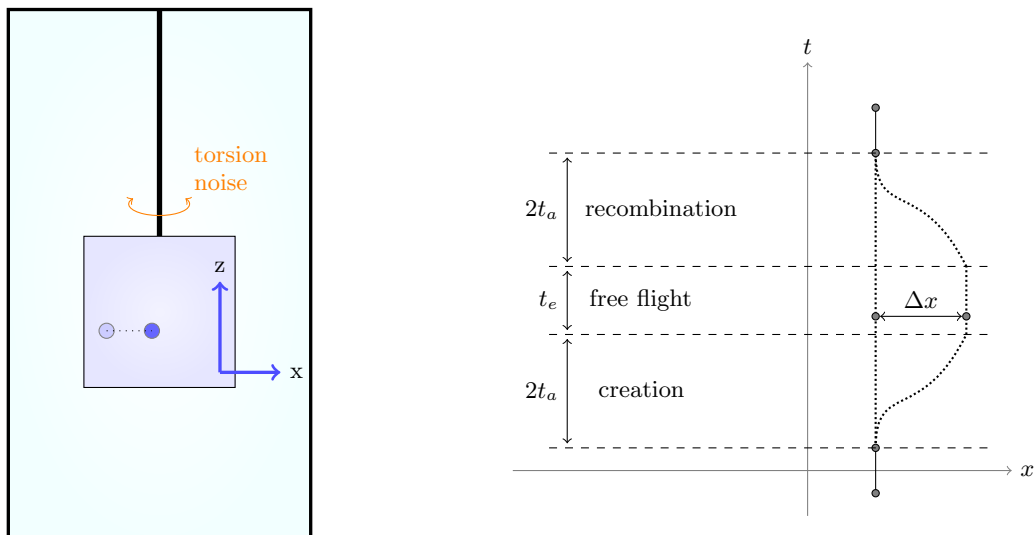
FIG. 1. (a) Experimental scheme and illustration of inertial torsion noise (ITN). The matter-wave particle (light and dark blue circles) is placed inside the experimental box (blue box), which is suspended by a thin wire (black vertical line). The box can rotate around the z-axis, while the interferometric protocol is performed along the horizontal x-axis. ITN generates random torques on the experimental box (blue rectangle), placing it in non-inertial rotational motion. The random non-inertial rotational motion induces random relative phases, which can lead to dephasing and the loss of interferometric contrast. (b) The structure of a Stern-Gerlach interferometer with spin-1 [25]. The left path keeps the same position, while the right path accelerates and decelerates at a constant rate, resulting in a superposition size Δx. Such motion is achieved using a constant magnetic field gradient, i.e. $B(x) = B_0 + \eta x$, where the gradient η is positive during $0 \sim t_a$ and $3t_a + t_e \sim 4t_a + t_e$, while it is negative during $t_a \sim 2t_a$ and $2t_a + t_e \sim 3t_a + t_e$. During the intermediate free flight of duration t_e, the magnetic field is uniform, and the right path does not accelerate. Such an asymmetrically shaped interferometer can be used to detect gravity-gradients [21, 35, 36]

can cause a sensitivity loss on the measurement result of g, then one can obtain a constrain for Γ by the variance σ_g of δg as $\sqrt{\Gamma} = 16\pi m\sigma_g\Delta z/(\hbar\omega_0)$, as long as $\delta\phi_{\text{diff}}$ and δg follow Gaussian distribution. Choosing the values as $m \sim 10^{-16}$ kg, $\Delta z \sim 10^{-8}$ m [47], then one may obtain a threshold as $\sqrt{\Gamma} < \sigma_g 10^7$ s^2/m. A common performance of gravimeters is $\sigma_g = 10^{-9} \sim 10^{-10}g$ [47], then one can choose the threshold of Γ as 10^{-6}.

- Another example is the QGEM experiment [35, 38], which uses two interferometers coupled by gravity to investigate gravity-induced quantum entanglement. The witness $\hat{W}$ is proposed as the positive partial transpose (PPT) witness, which, in the case of two qubits, provides a sufficient and necessary condition for entanglement based on the Peres-Horodecki criterion [48–50], which requires the expectation value of the witness satisfying $\langle\hat{W}\rangle < 0$. As is calculated in [38], the expectation value of the witness under the dephasing effect is $\langle\hat{W}\rangle = (1 - e^{-2\Gamma})/4 - e^{-\Gamma/2}\sin\phi_g$, then the constrain on Γ is that $\Gamma/2 < e^{-\Gamma/2}\sin\phi_g \approx \phi_g$. The value of ϕ_g has been estimated as $\phi_g \approx 0.015$ [35, 51], then we will choose a threshold $\Gamma = 0.01$ for further discussions on the values of parameters in this paper.

Dephasing, together with all other types of decoher-

ence, can be also characterized by computing the purity:

$$\text{Tr}(\mathbb{E}[\hat{\rho}]^2) = \frac{1}{2}(1 + e^{-2\Gamma}) \approx 1 - \Gamma. \tag{4}$$

Note that the dephasing comes from the ensemble average of the density matrix. In particular, $\text{Tr}(\hat{\rho}^2)$ without ensemble average still equals 1. We will refer to Γ as the *dephasing factor* in the following text. In the next section, we will analyze the dephasing factor Γ caused by the ITN.

III. DEPHASING AS LINEAR RESPONSE TO INERTIAL TORSION NOISE

As is derived in Appendix A, the Lagrangian of the inertial torsion noise is given by

$$L_{\text{ITN}} = \frac{1}{2}m\dot{\Theta}^2 x^2, \tag{5}$$

where m and x are the interferometer's mass and position, and $\Theta(t)$ is the torsion angle of the suspended apparatus, i.e., the angle between the apparatus reference frame and the inertial reference frame.

The angle $\Theta(t)$ is assumed to be a stochastic Gaussian

process, satisfying the following two properties:

$$\mathbb{E}[\Theta(t)] = 0$$

$$\mathbb{E}[\Theta(t_1)\Theta(t_2)] = \int S_{\Theta\Theta}(\omega)e^{-i\omega(t_2-t_1)}d\omega \tag{6}$$

where $S_{\Theta\Theta}(\omega)$ is the *power spectrum density* (PSD) of $\Theta(t)$ and the second identity is known as the Wiener-Khinchin theorem. The PSD of Θ can be measured in the experiment. In this paper, we will consider a specific source of fluctuation of Θ (e.g., the collision by gas molecules, which will discussed in the next section).

As is proved in [52, 53], the phase fluctuations due to noises are determined by the path integral of the corresponding Lagrangian of the noise along the unperturbed classical trajectories. Thus, the phase fluctuation is

$$\delta\phi = \frac{1}{\hbar} \int L_{\text{ITN}}[x_R(t)] - L_{\text{ITN}}[x_L(t)]dt$$

$$= \frac{m}{2\hbar} \int \dot{\Theta}^2(t) \left(x_R^2(t) - x_L^2(t)\right) dt, \tag{7}$$

where $x_R(t)$ and $x_L(t)$ are the trajectories of the interferometer's two arms. Assuming the expectation value of $\delta\phi$ vanishes, and the variance $\Gamma \equiv \mathbb{E}[(\delta\phi)^2]$ of the random phase can be regarded as the linear response of the interferometer to the torsion noise [35]:

$$\Gamma = \frac{m^2}{4\hbar^2} \int S_{\dot{\Theta}^2\dot{\Theta}^2}(\omega)F(\omega)d\omega, \tag{8}$$

where $S_{\dot{\Theta}^2\dot{\Theta}^2}(\omega)$ is the PSD of the ITN. According to the Wiener-Khinchin theorem, the PSD is the Fourier transform of the autocorrelation function of the torsion noise

$$S_{\dot{\Theta}^2\dot{\Theta}^2}(\omega) = \int \mathbb{E}[\dot{\Theta}^2(t_0)\dot{\Theta}^2(t_0 + \tau)]e^{i\omega\tau}d\tau. \tag{9}$$

Note that $S_{\dot{\Theta}^2\dot{\Theta}^2}(\omega)$ has a unit of Hz^4/Hz, where Hz^4 comes from the square of $\dot{\Theta}^2$ and the denominator Hz describes the density of frequency space. The $F(\omega)$ in Eq. (8) has the unit m^4s^2, and is given by

$$F(\omega) = \left| \int \left(x_R^2(t) - x_L^2(t)\right) e^{i\omega t}dt \right|^2. \tag{10}$$

Eq. (8) describes the input-output relation of the interferometer and only depends on the trajectories of the two arms, so it can be called the *transfer function* of the interferometer[36]. For the interferometer in Fig.1(b), the left arm is static $x_L(t) \equiv 0$, and the right arm $x_R(t)$ is described by a piecewise function consisting of several quadratic functions of t because the acceleration is $\pm a_m$ for the different time range. Then the transfer function can be computed as

$$F(\omega) = 16\frac{a_m^4}{\omega^{10}} \left[6\omega t_a \cos\left(\omega(t_a + \frac{t_e}{2})\right) + (\omega^2 t_a^2 + 3)\sin\frac{\omega t_e}{2} \right.$$

$$\left. - 3\sin\left(\omega(2t_a + \frac{t_e}{2})\right) - \omega^2 t_a^2 \sin\left(\omega(t_a + \frac{t_e}{2})\right) \right]^2. \tag{11}$$
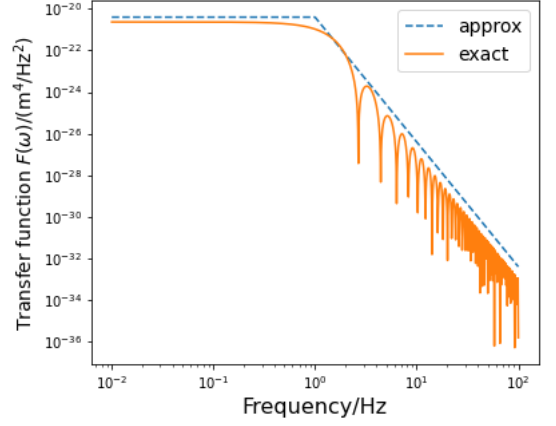

FIG. 2. Transfer function of the interferometer illustrated in Fig.1(b) as a function of the frequency $f = \omega/(2\pi)$. The time parameters are $t_a = 0.25\,\text{s}$ and $t_e = 0\,\text{s}$. The magnetic field gradient η is chosen as $10^4\,\text{T/m}$ and the mass of the interferometer is chosen as $10^{-15}\,\text{kg}$. The resulting acceleration $a_m = 1.8 \times 10^{-4}\,\text{m/s}^2$ produces the maximum superposition size $\Delta x = a_m t_a^2 = 11.2\,\mu\text{m}$. As is shown, the transfer function tends to a constant $C \sim (\Delta x)^4 T^2 \sim 10^{-20}\,\text{m}^4\text{s}^2$ at low frequencies, and decreases as ω^{-6} at high frequencies. The approximate transfer function from Eq. (14) (dashed blue line) captures the behaviour of the transfer function from Eq. (11) (orange line).

Fig.2 shows the transfer function with the parameters chosen as $t_a = 0.25\,\text{s}$, $t_e = 0\,\text{s}$ and $a_m = 1.8 \times 10^{-4}\,\text{m/s}^2$, where $a_m = g\mu_B\eta/m_0$ with the magnetic field gradient $\eta = 10^4\,\text{T/m}$ and the mass of the interferometer $m_0 = 10^{-15}\,\text{kg}$.

As is shown in Fig.2, $F(\omega)$ tends to a constant $C \sim (\Delta x)^4 T^2 \sim 10^{-20}\,\text{m}^4\text{s}^2$ in low frequency limit where $\Delta x = a_m t_a^2 = 11.2\,\mu\text{m}$ and $T = 4t_a + t_e$ are the superposition size and the total experiment time. It is because the factor $e^{i\omega t} \to 1$ in the low-frequency limit $\omega \to 0$, and the superposition size Δx is a upper bound for $x_R(t)$ when $x_L(t) \equiv 0$, so $F(\omega)$ in (10) can be approximated in low-frequency region as

$$F(\omega) \sim \left| \int (\Delta x)^2 dt \right|^2 = (\Delta x)^4 T^2. \tag{12}$$

At the high frequency limit, $F(\omega)$ decrease as ω^{-6}. In particular, the trajectory $x_R(t)$ can be generally expanded as a Taylor series of t with the leading order $x_R(t) \sim t$, so $x_R^2(t) \sim t^2$, then the leading order of $F(\omega)$ can be estimated according to (10) as

$$F(\omega) \sim \left| \int t^2 e^{i\omega t}dt \right|^2 \sim (\omega^{-3})^2 = \omega^{-6}. \tag{13}$$

Combining the low-frequency and high-frequency behaviours of $F(\omega)$, one can use the Heaviside step function

$\theta(\cdot)$ to approximately describe $F(\omega)$ as

$$F(\omega) \approx (\Delta x)^4 T^2 \left(\theta \left(\frac{2\pi}{T} - \omega \right) + \left(\frac{2\pi}{T\omega} \right)^6 \theta \left(\omega - \frac{2\pi}{T} \right) \right). \tag{14}$$

IV. POWER SPECTRUM DENSITY OF INERTIAL TORSION NOISE

In this section, we will analyze the inertial torsion noise caused by the thermal motion of gas molecules surrounding the experimental box.

According to the convolution theorem, the PSD of ITN is the self-convolution of the PSD of the random motion of the suspended apparatus

$$S_{\dot{\Theta}^2 \dot{\Theta}^2}(\omega) = S_{\dot{\Theta}\dot{\Theta}}(\omega) * S_{\dot{\Theta}\dot{\Theta}}(\omega), \tag{15}$$

where $S_{\dot{\Theta}\dot{\Theta}}(\omega)$ is the PSD of $\dot{\Theta}$. In frequency space, there is a correspondence that $\dot{\Theta} \sim \mathrm{i}\omega\Theta$, so the PSD of $\dot{\Theta}(t)$ is

$$S_{\dot{\Theta}\dot{\Theta}}(\omega) = \omega^2 S_{\Theta\Theta}(\omega). \tag{16}$$

As is shown in Fig. 1(a), the rotational motion of the experimental box can be modelled as a torsion pendulum, which follows a generalized Langevin equation

$$\ddot{\Theta} = -\Omega_{\mathrm{rot}}^2 \Theta - \gamma\dot{\Theta} + \sqrt{A}\Theta_{\mathrm{in}}(t). \tag{17}$$

The input random noise term $\Theta_{\mathrm{in}}(t)$ is a unit delta-correlated stationary Gaussian process with zero-mean, satisfying $\mathbb{E}[\Theta_{\mathrm{in}}(t)] = 0$ at any time t, and $\mathbb{E}[\Theta_{\mathrm{in}}(t_1)\Theta_{\mathrm{in}}(t_2)] = \delta(t_1 - t_2)$. The amplitude of the external noise $\sqrt{A}$ [1] and the dissipation rate γ are determined by the experiment. The intrinsic torsion frequency is given by [54]

$$\Omega_{\mathrm{rot}} = \sqrt{\frac{\kappa}{I}} = \sqrt{\frac{\pi\mathbb{G}d^4}{32lI}}, \tag{18}$$

where I is the moment of inertia of the experiment box and $\kappa = \sqrt{\pi\mathbb{G}d^4/32l}$ is the torsion constant. $\mathbb{G}$ is the shear modulus of the material of the suspension wire, d and l are the diameter and the length of the wire. The size and the mass of the experiment box can be built up as $10^{-1} \sim 10^0$ m and $10^1 \sim 10^2$ kg, so the moment of inertia I can be estimated as $10^0 \sim 10^2$ kg·m^2. The parameters of the suspension wire are around $d = 10^{-3} \sim 10^{-2}$ m, $l = 10^0 \sim 10^1$ m and $\mathbb{G} \sim 10^{10}$ Pa, then the intrinsic frequency Ω_{rot} of the torsion pendulum is around $10^{-2} \sim 10^1$ Hz.
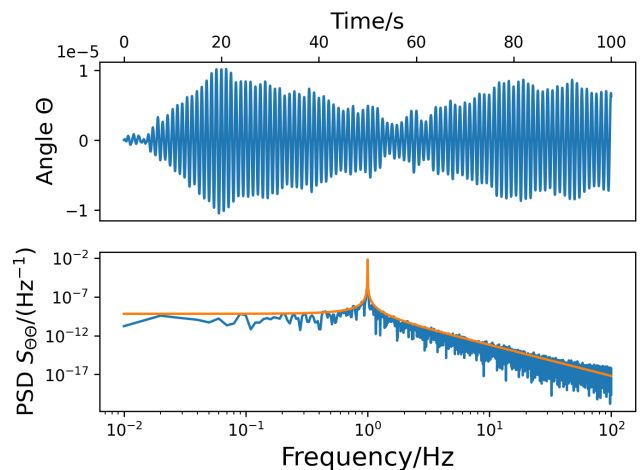

FIG. 3. Monte Carlo simulation for the motion of the box. (a) Simulated time-trace of Eq. (C1). (b) The PSD $S_{\Theta\Theta}(\omega)$ in the lower plot is computed by FFT. Theoretically the PSD is a Lorentzian distribution which fits the simulation result well. The intrinsic frequency Ω_{rot} is chosen as $2\pi \times 1$ Hz, the damping rate γ is chosen as 10^{-10} Hz and the noise amplitude $\sqrt{A}$ is chosen as 10^{-3} Hz$^2/\sqrt{\mathrm{Hz}}$

For example, if the experiment box is built up with size $L = 0.6$ m and mass $M = 30$ kg, then the moment of inertia is $I = ML^2/6 = 1.8$ kg·m^2. If the suspension wire is set as $d = 5 \times 10^{-3}$ m and $l = 5$ m, and the shear modulus is chosen as $\mathbb{G} = 7.93 \times 10^{10}$ Pa for steel [55], then the intrinsic torsion frequency is $\Omega_{\mathrm{rot}} \approx 0.735$ Hz according to Eq. (18).

Based on the dynamical equation (17) of the experiment box, the power spectrum for Θ is [2]

$$S_{\Theta\Theta}(\omega) = \frac{A}{(\Omega_{\mathrm{rot}}^2 - \omega^2)^2 + \gamma^2\omega^2}. \tag{19}$$

One may do a Monte Carlo simulation of the Langevin equation given in Eq. (17), shown as the upper figure of Fig. 3, and calculate the corresponding PSD by fast Fourier transform (FFT), where a Hanning window has been added to avoid the spectral leakage, shown as the lower figure of Fig. 3. We find that the analytic result Eq. (19) matches well with the numerical result.

Since the PSD of ITN is the self-convolution of $S_{\dot{\Theta}\dot{\Theta}}(\omega)$ according to Eq. (15), one can compute the PSD of the

---

[1] Note that A is of the unit Hz^4/Hz. It is because the term $\sqrt{A}\Theta_{\mathrm{in}}(t)$ has a dimension $[\mathrm{T}^{-2}]$, where $\Theta_{\mathrm{in}}(t)$ has a dimension $[\mathrm{T}^{-1/2}]$.

[2] Here we used the result $S_{\mathrm{in}}(\omega) \equiv |\Theta_{\mathrm{in}}(\omega)|^2/T_{\mathrm{tot}} = 1$, which can be obtained through the auto-correction condition $\mathbb{E}[\Theta_{\mathrm{in}}(t_1)\Theta_{\mathrm{in}}(t_2)] = \delta(t_1 - t_2)$ and the Wiener-Khinchin theorem that

$$\frac{|\Theta_{\mathrm{in}}(\omega)|^2}{T_{\mathrm{tot}}} = \int \mathbb{E}[\Theta_{\mathrm{in}}(t)\Theta_{\mathrm{in}}(t+\tau)]\mathrm{e}^{\mathrm{i}\omega\tau}\mathrm{d}\tau$$
$$= \int \delta(\tau)\mathrm{e}^{\mathrm{i}\omega\tau}\mathrm{d}\tau = 1.$$

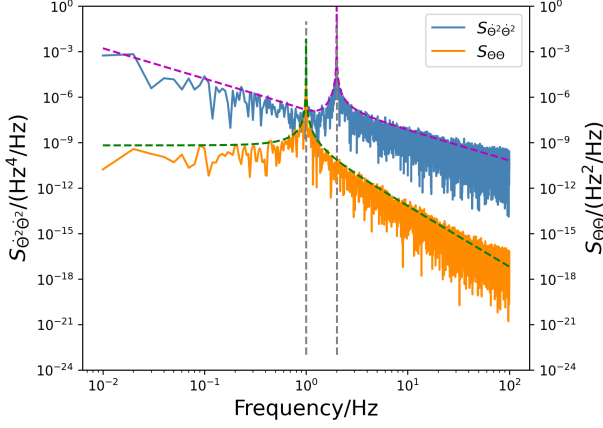FIG. 4. PSD of ITN $S_{\dot{\Theta}^2\dot{\Theta}^2}(\omega)$ and angular motion PSD $S_{\Theta\Theta}(\omega)$. The parameters are chosen as $\Omega_{\rm rot} = 2\pi \times 1\,{\rm Hz}$, $\gamma = 10^{-10}\,{\rm Hz}$, $I = 10\,{\rm kg \cdot m^2}$ and $\sqrt{A} = 10^{-3}\,{\rm Hz}^2/\sqrt{\rm Hz}$. . The peak frequency of $S_{\dot{\Theta}^2\dot{\Theta}^2}(\omega)$ is doubled compared to $S_{\Theta\Theta}(\omega)$ as expected when computing the square of the noise [3]. The dashed green and purple lines show that the theoretical expressions in Eqs. (19) and (20) fit well the simulated PSDs.

ITN driven by the external noise with the PSD given by Eq. (19) as

$$S_{\dot{\Theta}^2\dot{\Theta}^2}(\omega) = A^2 \frac{4\omega^4 + 4(\gamma^2 - 3\Omega_{\rm rot}^2)\omega^2 + 16\Omega_{\rm rot}^4}{\gamma(\omega^2 + \gamma^2)(4\gamma^2\omega^2 + (\omega^2 - 4\Omega_{\rm rot}^2)^2)}. \tag{20}$$

The detailed mathematical steps are summarized in Appendix B. Fig. 4 shows the analytical result and the numerical simulation of both $S_{\Theta\Theta}(\omega)$ and $S_{\dot{\Theta}^2\dot{\Theta}^2}(\omega)$.

The asymptotic behaviour of the PSD of ITN is different from the $S_{\Theta\Theta}(\omega)$. In low frequency limit, $S_{\dot{\Theta}^2\dot{\Theta}^2}(\omega)$ behaves like $1/(\omega^2 + \gamma_{\rm rot}^2)$ and tends to a constant A^2/γ. In high frequency region, $S_{\dot{\Theta}^2\dot{\Theta}^2}(\omega)$ decreases as ω^{-2} according to the analytic result (20).

There is also a peak of the PSD of ITN, of which the resonance frequency translates from $\Omega_{\rm rot}$ to $2\Omega_{\rm rot}$, which is a common property for a squared noise [3]. In a small damping limit $\gamma_{\rm rot} \ll \Omega_{\rm rot}$, the peak value of $S_{\dot{\Theta}^2\dot{\Theta}^2}(\omega)$

––––––––

[3] This property can be understood as follows. Since $S_{\dot{\Theta}\dot{\Theta}}$ has a peak at $\Omega_{\rm rot}$, then it can be written as a δ-function plus some small function $o(\omega)$:

$$S_{\dot{\Theta}\dot{\Theta}}(\omega) = S_0\delta(\omega - \Omega_{\rm rot}) + o(\omega),$$

where S_0 is the amplitude of the peak. Then the self-convolution of $S_{\dot{\Theta}\dot{\Theta}}$ gives

$$S_{\dot{\Theta}^2\dot{\Theta}^2}(\omega) = S_0^2 \int \delta(\omega' - \Omega_{\rm rot})\delta(\omega - \omega' - \Omega_{\rm rot}){\rm d}\omega' + o'(\omega)$$
$$= S_0^2\delta(\omega - 2\Omega_{\rm rot}) + o'(\omega),$$

which means the peak position locates at $2\Omega_{\rm rot}$. In Appendix B, we offer another method to understand this property in the time domain.

is

$$S_{\dot{\Theta}^2\dot{\Theta}^2}(2\Omega_{\rm rot}) \approx \frac{A^2}{2\gamma^3}. \tag{21}$$

It is notatble that

$$S_{\dot{\Theta}^2\dot{\Theta}^2}(2\Omega_{\rm rot} \pm \gamma) \approx \frac{A^2}{4\gamma^3}. \tag{22}$$

So the frequency at which the PSD equals to the half peak value are $\omega = 2\Omega_{\rm rot} \pm \gamma$ and the corresponding full width at half maximum (FWHM) is 2γ. The radio between the bandwidth and the peak value is known as the quality factor (Q-factor) of the PSD, which characterizes the sharpness of the peak. Then the Q-factor of $S_{\dot{\Theta}^2\dot{\Theta}^2}(\omega)$ is

$$Q_{\rm ITN} = \frac{2\Omega_{\rm rot}}{2\gamma} = \frac{\Omega_{\rm rot}}{\gamma}, \tag{23}$$

which is exactly the same as the Q-factor of $S_{\Theta\Theta}(\omega)$.

V. DEPHASING FACTOR AND EXPERIMENT PARAMETERS CONSTRAIN

Based on the result of the transfer function in Eq. (11) or Eq. (14), and the power spectrum density (20) of the inertial torsion noise, the dephasing factor Γ can be computed through the integral in Eq. (8). Note that the analytic solution to the integral is very complicated, so we compute it numerically. It is noteworthy that a resolution of $\omega_{\rm min} = 2\pi/T_{\rm tot}$ exists as a cutoff in frequency space for the numerical calculation. Physically, this cutoff indicates that a low-frequency signal or noise will not be measurable by the experiment if the total experiment time is shorter than a single period of such signal or noise.

Fig. 5 shows the dependence of Γ on the intrinsic torsion frequency $\Omega_{\rm rot}$ of the experiment apparatus, where the parameters of $F(\omega)$ are chosen as $m_0 = 10^{-15}\,{\rm kg}$, $t_a = 0.25\,{\rm s}$ and $t_e = 0\,{\rm s}$, and the parameters of $S_{\dot{\Theta}^2\dot{\Theta}^2}(\omega)$ are $A = 10^{-10}\,{\rm Hz}^4/{\rm Hz}$ and $\gamma = 10^{-10}\,{\rm Hz}$. As is shown, there is a resonance between the ITN and the transfer function near $\Omega_{\rm rot} \sim 2\pi/T_{\rm tot} = 2\pi \times 1\,{\rm Hz}$ and some harmonic resonances. Note that near the resonance peak, the precision of the numerical calculation is limited because the value is highly related to the sample points in frequency space.

When $\Omega_{\rm rot}$ is much larger than $2\pi \times 10^0\,{\rm Hz}$, Γ becomes approximately independent on $\Omega_{\rm rot}$. On the other hand, when $\Omega_{\rm rot}$ is much smaller than $2\pi \times 10^{-1}\,{\rm Hz}$, the peak will be below the frequency cut-off $\omega_{\rm min}$, so the dephasing factor will be tiny. For an actual experiment, the low intrinsic frequency limit is expected, so the parameters d, l, $\mathbb{G}$ and I in (18) have to be carefully designed to ensure $\Omega_{\rm rot}$ much smaller than the resonance frequency $2\pi/T$ of the interferometer.

Fig. 6 shows the dependence of Γ on the damping rate γ. As is shown, when the damping rate is very low, i.e.
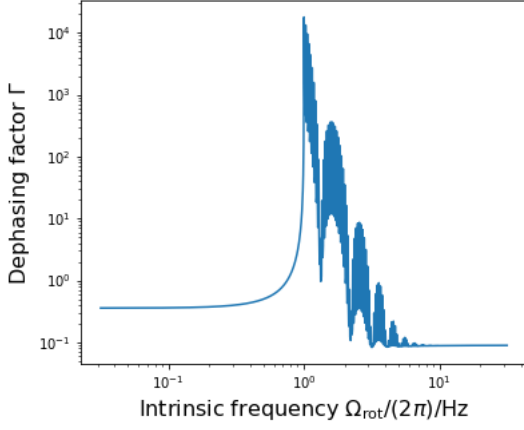
FIG. 5. Dephasing factor Γ as a function of the intrinsic torsion frequency $\Omega_{\rm rot}$. The parameters are chosen as $m_0 = 10^{-15}\,{\rm kg}$, $\eta = 10^4\,{\rm T/m}$, $t_a = 0.25\,{\rm s}$ and $t_e = 0\,{\rm s}$ for the interferometer, and $\gamma = 10^{-10}\,{\rm Hz}$, $I = 10\,{\rm kg \cdot m^2}$ and $A = 10^{-10}\,{\rm Hz^4/Hz}$ for the PSD of ITN. There is a resonance between the ITN and the transfer function with the first dominant peak at $\Omega_{\rm rot} \sim 2\pi/T_{\rm tot} \sim 2\pi \times 1\,{\rm Hz}$, and additional smaller peaks visible in the range upto 10. In the low frequency limit and high frequency limit, the dephasing factor Γ is approximately independent of the intrinsic frequency $\Omega_{\rm rot}$.
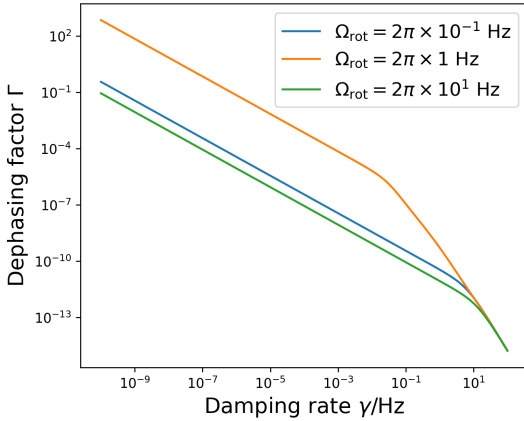

FIG. 6. The relationship between Γ and the damping factor γ for a fixed amplitude $A = 10^{-10}\,{\rm Hz^3}$. The transfer function is given in Eq. (11) with parameters $t_a = 0.25\,{\rm s}$ and $t_e = 0\,{\rm s}$. Three different $\Omega_{\rm rot}$ are chosen as the low rotation frequency limit, the high rotation frequency limit and the resonance frequency condition $\Omega_{\rm rot} \sim 2\pi/T = 2\pi\,{\rm Hz}$. Γ is proportional to γ^{-1} when $\gamma \ll \Omega_{\rm rot}$, while it decreases as a speed of γ^{-3} in the overdamped region.

$\gamma \ll \Omega_{\rm rot}$, the dephasing parameter Γ is approximately proportional to γ^{-1} due to the γ^{-1} factor in (20).

However, when γ increases after a critical point $\gamma \sim \Omega_{\rm rot}$, the dephasing Γ is approximately γ^{-3}. This is because the PSD of ITN at the high damping rate limit
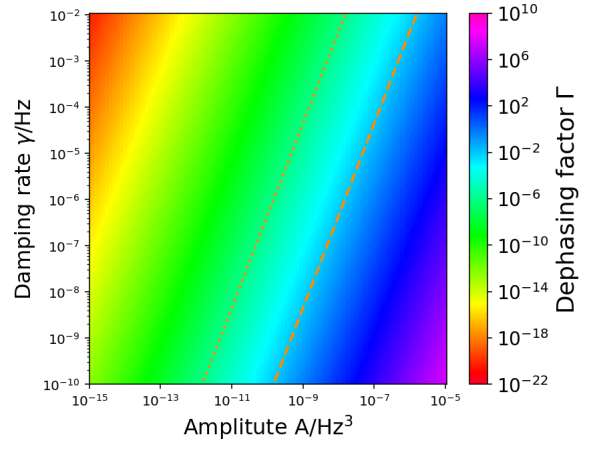

FIG. 7. The dephasing parameter Γ with respect to different damping rates γ and torsion noise amplitudes A. The transfer function is given by Eq. (11) with parameters $t_a = 0.25\,{\rm s}$ and $t_e = 0\,{\rm s}$, and the intrinsic frequency is chosen as $\Omega_{\rm rot} = 2\pi \times 1\,{\rm Hz}$. Γ is required smaller than some thresholds in different situations, then the parameters should be chosen on the left side of the critical lines in the figure, where the dotted and dashed lines represent $\Gamma = 10^{-6}$ and $\Gamma = 0.01$ for gravimeters and QGEM experiment in respect.

$\gamma \gg \Omega_{\rm rot}$ is approximately

$$S_{\dot\Theta^2\dot\Theta^2}(\omega) \approx A^2 \frac{4\omega^4 + 4\gamma_{\rm rot}^2\omega^2}{\gamma(\omega^2 + \gamma^2)(\omega^4 + 4\gamma^2\omega^2)} \sim \frac{A^2}{\gamma^3}. \quad (24)$$

Physically it can be interpreted as an overdamped oscillator. In particular, the apparatus's dynamical equation in Eq. (17) describes a damped oscillator under a randomly driven force. When the damping rate is larger than a critical value $\gamma > \Omega_{\rm rot}/2$, the system decays with no oscillation, known as overdamped. In the overdamped region, as the damping rate increases, the system decays to the equilibrium faster, so the random force term affects the system less. Finally, the dephasing parameter Γ decreases as the damping rate γ increases.

Fig. 7 shows the dependence of the dephasing parameter Γ concerning different damping rates γ and torsion noise amplitude A, where the parameters are chosen as $t_a = 0.25\,{\rm s}$ and $t_e = 0\,{\rm s}$ and $\Omega_{\rm rot} = 2\pi \times 1\,{\rm Hz}$. As is shown, Γ increases as A increases or γ decreases. As is discussed in section 2, the gravimeter and QGEM experiments require an upper bound of Γ as 10^{-6} and 0.01, then A and γ should be chosen in the region on the left side of the dotted and dashed critical line respectively in the figure.

Fig. 8 shows the upper bound of the torsion noise amplitude A to obtain a dephasing parameter Γ smaller than 0.01, where the parameters are also chosen as $t_a = 0.25\,{\rm s}$ and $t_e = 0\,{\rm s}$. Since Γ is proportional to A^2, so one can also use Fig. 8 to analyze other threshold of Γ by multiplying a factor on A. For example, one can analyze the case $\Gamma < 10^{-6}$ for gravimeters by multiplying 10^{-2} to the upper bound of A.
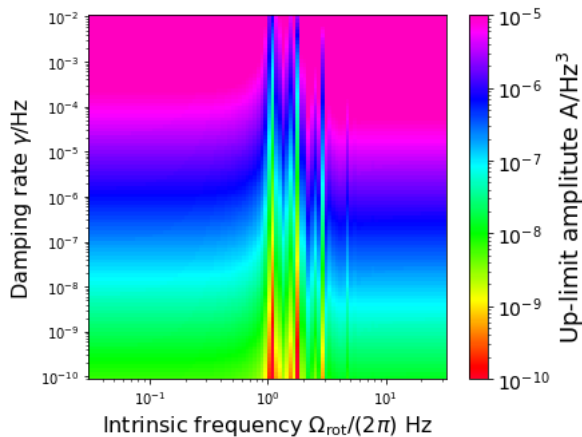
FIG. 8. The upper bound of the amplitude A assuming the value of the dephasing to be $\Gamma = 0.01$. The transfer function is is given by Eq. (11) with parameters $t_a = 0.25\,\mathrm{s}$ and $t_e = 0\,\mathrm{s}$. Near the resonance region $\Omega_{\mathrm{rot}} \sim 2\pi/T_{\mathrm{tot}} = 2\pi \times 1\,\mathrm{Hz}$ and its harmonic resonance $\Omega_{\mathrm{rot}} \sim 2n\pi/T_{\mathrm{tot}}$ (with n a positive integer), the upper bound of A becomes more constrained. On the other hand, the requirements on A relax outside the resonance region.

As is shown, the restriction on the upper bound of A is very stringent near the resonance region $\Omega_{\mathrm{rot}} \sim 2\pi/T_{\mathrm{tot}} = 2\pi \times 1\,\mathrm{Hz}$ and its harmonic resonance $\Omega_{\mathrm{rot}} \sim 2n\pi/T_{\mathrm{tot}}$ (with n a positive integer). In particular, A has to be smaller than $10^{-10}\,\mathrm{Hz}^3$ for $\gamma = 10^{-10}\,\mathrm{Hz}$, and it has to be smaller than $10^{-8}\,\mathrm{Hz}^3$ for $\gamma = 10^{-2}\,\mathrm{Hz}$. On the other hand, the value of A is less severely constrained outside the resonance region. For a damping rate larger than $10^{-4}\,\mathrm{Hz}$, A can be larger than $10^{-5}\,\mathrm{Hz}^3$.

In a recent simulation work [56], a relationship between the torsion noise amplitude A and the superposition size Δx has been obtained as $\Delta x A \sim 10^{-11}\,\mathrm{m} \cdot \mathrm{Hz}^3$. Since the superposition size discussed in this paper is $\Delta x = a_m t_a^2 = 11.2\,\mu\mathrm{m}$, then the noise amplitude is $A \sim 10^{-6}\,\mathrm{Hz}^3$, which is smaller than the restricted bound $A_{\mathrm{bound}} \sim 10^{-5}\,\mathrm{Hz}^3$. In conclusion, as long as the damping rate is designed to be larger than $10^{-4}\,\mathrm{Hz}$ and the intrinsic frequency Ω_{rot} is designed outside the resonance region, the dephasing parameter Γ of the interferometer will be smaller than 0.01.

VI. SUMMARY

In this paper, we investigated inertial torsion noise (ITN) in the context of matter-wave interferometry, and some of our highlights and conclusions are summarized below.

In section II, we explained the physical interpretation of the ITN and briefly reviewed the dephasing effect of generic noises on matter-wave interferometers. The key point is that the ensemble average of a random phase implies a decay factor $\mathbb{E}[e^{i\delta\phi}] = e^{-\Gamma}$ on the off-diagonal terms of the density matrix, where the dephasing parameter is exactly the variance of the noise $\Gamma = \mathbb{E}[(\delta\phi)^2]$.

In section III, we pointed out that the decay factor Γ can be regarded as a linear response of the interferometer to the ITN. In particular, Γ can be formulated as the PSD of the noise $S_{\dot{\Theta}^2 \dot{\Theta}^2}(\omega)$ multiplying a transfer function $F(\omega)$ in frequency space. Remarkably, $F(\omega)$ only relies on the trajectories of the two arms of the interferometer and is independent of the noise. In the rest part of section 3, some asymptotic features of $F(\omega)$ are discussed, and the exact and approximate result for a certain interferometer is shown as Fig. 2.

In section IV, we modelled the torsion noise by a generalized Langevin equation (17), which implies the PSD $S_{\Theta\Theta}(\omega)$ as (19). Then the PSD of the ITN $S_{\dot{\Theta}^2 \dot{\Theta}^2}(\omega)$ is the self-convolution of $S_{\dot{\Theta}\dot{\Theta}}(\omega)$ according to the convolution theorem, where the math details are summarized in Appendix B. It is remarkable that the peak position of $S_{\dot{\Theta}^2 \dot{\Theta}^2}(\omega)$ is doubled compared to $S_{\dot{\Theta}\dot{\Theta}}(\omega)$ because of properties of self-convolution, while the Q-factor of $S_{\dot{\Theta}^2 \dot{\Theta}^2}(\omega)$ remains the same as $S_{\dot{\Theta}\dot{\Theta}}(\omega)$.

In section V, we scanned parameters theoretically and found some major features as follows. First, Γ increases significantly near the resonance region $\Omega_{\mathrm{rot}} = 2n\pi/T_{\mathrm{tot}}$. Next, Γ descreases proportional to the damping rate γ^{-1} in the underdamped region, while it decreases with γ^{-3} in the overdamped region. Finally, if Γ is required smaller than 0.01, then constrain on the parameters A, γ and Ω_{rot} shown as Fig.8, and A is tolerant up to $10^{-5}\,\mathrm{Hz}^3$ if $\gamma > 10^{-4}\,\mathrm{Hz}$ and Ω_{rot} is outside the resonance region.

ACKNOWLEDGMENTS

[1] Achim Peters, Keng Yeow Chung, and Steven Chu. Measurement of gravitational acceleration by dropping atoms. *Nature*, 400(6747):849–852, Aug 1999.

[2] J. B. Fixler, G. T. Foster, J. M. McGuirk, and M. A. Kasevich. Atom interferometer measurement of the newtonian constant of gravity. *Science*, 315(5808):74–77, 2007.

[3] Ben Stray, Andrew Lamb, Aisha Kaushik, Jamie Vovrosh, Anthony Rodgers, Jonathan Winch, Farzad Hayati, Daniel Boddice, Artur Stabrawa, Alexander Niggebaum, Mehdi Langlois, Yu-Hung Lien, Samuel Lellouch, Sanaz Roshanmanesh, Kevin Ridley, Geoffrey de Villiers, Gareth Brown, Trevor Cross, George Tuckwell, Asaad Faramarzi, Nicole Metje, Kai Bongs, and Michael Holynski. Quantum sensing for gravity cartography. *Nature*, 602(7898):590–594, Feb 2022.

[4] Jack C. Saywell, Max S. Carey, Philip S. Light, Stuart S. Szigeti, Alistair R. Milne, Karandeep S. Gill, Matthew L. Goh, Viktor S. Perunicic, Nathanial M. Wilson, Calum D. Macrae, Alexander Rischka, Patrick J. Everitt, Nicholas P. Robins, Russell P. Anderson, Michael R. Hush, and Michael J. Biercuk. Enhancing the sensitivity of atom-interferometric inertial sensors using robust control. *Nature Communications*, 14(1):7626, Nov 2023.

[5] Vladimir V. Soshenko, Stepan V. Bolshedvorskii, Olga Rubinas, Vadim N. Sorokin, Andrey N. Smolyaninov, Vadim V. Vorobyov, and Alexey V. Akimov. Nuclear spin gyroscope based on the nitrogen vacancy center in diamond. *Phys. Rev. Lett.*, 126:197702, May 2021.

[6] Chris Overstreet, Peter Asenbaum, Tim Kovachy, Remy Notermans, Jason M. Hogan, and Mark A. Kasevich. Effective inertial frame in an atom interferometric test of the equivalence principle. *Phys. Rev. Lett.*, 120:183604, May 2018.

[7] Peter Asenbaum, Chris Overstreet, Minjeong Kim, Joseph Curti, and Mark A. Kasevich. Atom-interferometric test of the equivalence principle at the 10^{-12} level. *Phys. Rev. Lett.*, 125:191101, Nov 2020.

[8] Sougato Bose, Anupam Mazumdar, Martine Schut, and Marko Toroš. Entanglement witness for the weak equivalence principle. *Entropy*, 25(3):448, 2023.

[9] Sougato Bose, Anupam Mazumdar, Gavin W. Morley, Hendrik Ulbricht, Marko Toroš, Mauro Paternostro, Andrew A. Geraci, Peter F. Barker, M. S. Kim, and Gerard Milburn. Spin entanglement witness for quantum gravity. *Phys. Rev. Lett.*, 119:240401, Dec 2017.

[10] Sougato Bose. *https://www.youtube.com/watch?v=0Fv-0k13s_k*, 2016. Accessed 1/11/22, on behalf of QGEM collaboration.

[11] C. Marletto and V. Vedral. Gravitationally induced entanglement between two massive particles is sufficient evidence of quantum effects in gravity. *Phys. Rev. Lett.*, 119:240402, Dec 2017.

[12] Ryan J. Marshman, Anupam Mazumdar, and Sougato Bose. Locality and entanglement in table-top testing of the quantum nature of linearized gravity. *Phys. Rev. A*, 101(5):052110, 2020.

[13] Daniel Carney. Newton, entanglement, and the graviton. *Phys. Rev. D*, 105(2):024029, 2022.

[14] Dripto Biswas, Sougato Bose, Anupam Mazumdar, and Marko Toroš. Gravitational optomechanics: Photon-matter entanglement via graviton exchange. *Phys. Rev. D*, 108(6):064023, 2023.

[15] Shafaq Gulzar Elahi and Anupam Mazumdar. Probing massless and massive gravitons via entanglement in a warped extra dimension. *Phys. Rev. D*, 108(3):035018, 2023.

[16] Ulrich K. Beckering Vinckers, Álvaro de la Cruz-Dombriz, and Anupam Mazumdar. Quantum entanglement of masses with nonlocal gravitational interaction.

[17] Canuel, B., Amand, L., Bertoldi, A., Chaibi, W., Geiger, R., Gillot, J., Landragin, A., Merzougui, M., Riou, I., Schmid, S.P., and Bouyer, P. The matter-wave laser interferometer gravitation antenna (miga): New perspectives for fundamental physics and geosciences. *E3S Web of Conferences*, 4:01004, 2014.

[18] J. Junca, A. Bertoldi, D.O. Sabulsky, G. Lefèvre, X. Zou, J.-B. Decitre, R. Geiger, A. Landragin, S. Gaffet, P. Bouyer, and B. Canuel. Characterizing earth gravity field fluctuations with the miga antenna for future gravitational wave detectors. *Physical Review D*, 99(10), May 2019.

[19] Mahiro Abe, Philip Adamson, Marcel Borcean, Daniela Bortoletto, Kieran Bridges, Samuel P Carman, Swapan Chattopadhyay, Jonathon Coleman, Noah M Curfman, Kenneth DeRose, Tejas Deshpande, Savas Dimopoulos, Christopher J Foot, Josef C Frisch, Benjamin E Garber, Steve Geer, Valerie Gibson, Jonah Glick, Peter W Graham, Steve R Hahn, Roni Harnik, Leonie Hawkins, Sam Hindley, Jason M Hogan, Yijun Jiang, Mark A Kasevich, Ronald J Kellett, Mandy Kiburg, Tim Kovachy, Joseph D Lykken, John March-Russell, Jeremiah Mitchell, Martin Murphy, Megan Nantel, Lucy E Nobrega, Robert K Plunkett, Surjeet Rajendran, Jan Rudolph, Natasha Sachdeva, Murtaza Safdari, James K Santucci, Ariel G Schwartzman, Ian Shipsey, Hunter Swan, Linda R Valerio, Arvydas Vasonis, Yiping Wang, and Thomas Wilkason. Matter-wave atomic gradiometer interferometric sensor (magis-100). *Quantum Science and Technology*, 6(4):044003, jul 2021.

[20] Jeremiah Thomas Mitchell, Tim Kovachy, Steve Hahn, Philip Adamson, and Swapan Chattopadhyay. MAGIS-100 environmental characterization and noise analysis. *JINST*, 17(01):P01007, 2022. [Erratum: JINST 17, E02001 (2022)].

[21] Ryan J Marshman, Anupam Mazumdar, Gavin W Morley, Peter F Barker, Steven Hoekstra, and Sougato Bose. Mesoscopic interference for metric and curvature and gravitational wave detection. *New Journal of Physics*, 22(8):083012, aug 2020.

[22] Thomas W. van de Kamp, Ryan J. Marshman, Sougato Bose, and Anupam Mazumdar. Quantum Gravity Witness via Entanglement of Masses: Casimir Screening. *Phys. Rev. A*, 102(6):062807, 2020.

[23] Martine Schut, Andrew Geraci, Sougato Bose, and Anupam Mazumdar. Micrometer-size spatial superpositions for the qgem protocol via screening and trapping. *Phys. Rev. Res.*, 6:013199, Feb 2024.

[24] Martine Schut, Alexey Grinin, Andrew Dana, Sougato Bose, Andrew Geraci, and Anupam Mazumdar. Relaxation of experimental parameters in a quantum-gravity-induced entanglement of masses protocol using electromagnetic screening. *Phys. Rev. Res.*, 5(4):043170, 2023.

[25] Mark Keil, Shimon Machluf, Yair Margalit, Zhifan Zhou, Omer Amit, Or Dobkowski, Yonathan Japha, Samuel Moukouri, Daniel Rohrlich, Zina Binstock, Yaniv Bar-Haim, Menachem Givon, David Groswasser, Yigal Meir, and Ron Folman. *Stern-Gerlach Interferometry with the Atom Chip*, pages 263–301. Springer International Publishing, Cham, 2021.

[26] Shimon Machluf, Yonathan Japha, and Ron Folman. Coherent Stern–Gerlach momentum splitting on an atom chip. *Nature Communications*, 4(1):2424, September

2013.

[27] Shimon Machluf, Yonathan Japha, and Ron Folman. Coherent stern–gerlach momentum splitting on an atom chip. *Nature Communications*, 4(1):2424, Sep 2013.

[28] Yair Margalit, Or Dobkowski, Zhifan Zhou, Omer Amit, Yonathan Japha, Samuel Moukouri, Daniel Rohrlich, Anupam Mazumdar, Sougato Bose, Carsten Henkel, and Ron Folman. Realization of a complete stern-gerlach interferometer: Toward a test of quantum gravity. *Science Advances*, 7(22):eabg2879, 2021.

[29] C. Wan, M. Scala, G. W. Morley, ATM. A. Rahman, H. Ulbricht, J. Bateman, P. F. Barker, S. Bose, and M. S. Kim. Free nano-object ramsey interferometry for large quantum superpositions. *Phys. Rev. Lett.*, 117:143003, Sep 2016.

[30] Julen S. Pedernales, Gavin W. Morley, and Martin B. Plenio. Motional dynamical decoupling for interferometry with macroscopic particles. *Phys. Rev. Lett.*, 125:023602, Jul 2020.

[31] Ryan J. Marshman, Anupam Mazumdar, Ron Folman, and Sougato Bose. Constructing nano-object quantum superpositions with a stern-gerlach interferometer. *Phys. Rev. Res.*, 4:023087, May 2022.

[32] Run Zhou, Ryan J. Marshman, Sougato Bose, and Anupam Mazumdar. Catapulting towards massive and large spatial quantum superposition. *Phys. Rev. Res.*, 4:043157, Dec 2022.

[33] Run Zhou, Ryan J. Marshman, Sougato Bose, and Anupam Mazumdar. Mass-independent scheme for enhancing spatial quantum superpositions. *Phys. Rev. A*, 107:032212, Mar 2023.

[34] André Großardt. Acceleration noise constraints on gravity-induced entanglement. *Phys. Rev. A*, 102:040202, Oct 2020.

[35] Marko Toroš, Thomas W. van de Kamp, Ryan J. Marshman, M. S. Kim, Anupam Mazumdar, and Sougato Bose. Relative acceleration noise mitigation for nanocrystal matter-wave interferometry: Applications to entangling masses via quantum gravity. *Phys. Rev. Research*, 3:023178, Jun 2021.

[36] Meng-Zhi Wu, Marko Toroš, Sougato Bose, and Anupam Mazumdar. Quantum gravitational sensor for space debris. *Phys. Rev. D*, 107:104053, May 2023.

[37] Paolo Fragolino, Martine Schut, Marko Toroš, Sougato Bose, and Anupam Mazumdar. Decoherence of a matter-wave interferometer due to dipole-dipole interactions. *Phys. Rev. A*, 109:033301, Mar 2024.

[38] Martine Schut, Herre Bosma, MengZhi Wu, Marko Toroš, Sougato Bose, and Anupam Mazumdar. Dephasing due to electromagnetic interactions in spatial qubits. *Phys. Rev. A*, 110:022412, Aug 2024.

[39] Marko Toroš, Anupam Mazumdar, and Sougato Bose. Loss of coherence and coherence protection from a graviton bath. *Phys. Rev. D*, 109:084050, Apr 2024.

[40] Gregory M Harry, forthe LIGO Scientific Collaboration, et al. Advanced ligo: the next generation of gravitational wave detectors. *Classical and Quantum Gravity*, 27(8):084006, 2010.

[41] G. Losurdo, M. Bernardini, S. Braccini, C. Bradaschia, C. Casciano, V. Dattilo, R. De Salvo, A. Di Virgilio, F. Frasconi, A. Gaddi, A. Gennai, A. Giazotto, H. B. Pan, F. Paoletti, A. Pasqualetti, R. Passaquieti, D. Passuello, R. Taddei, Z. Zhang, G. Cella, E. Cuoco, E. D'Ambrosio, F. Fidecaro, S. Gaggero, P. La Penna, S. Mancini, R. Poggiani, A. Vicerè, M. Mazzoni, R. Stanga, L. Holloway, and J. Winterflood. An inverted pendulum preisolator stage for the VIRGO suspension system. *Review of Scientific Instruments*, 70(5):2507–2515, 05 1999.

[42] Peter R. Saulson, Robin T. Stebbins, Frank D. Dumont, and Scott E. Mock. The inverted pendulum as a probe of anelasticity. *Review of Scientific Instruments*, 65(1):182–191, 01 1994.

[43] Jean-Charles Dumas, Li Ju, and David G. Blair. Modelling of tuning of an ultra low frequency roberts linkage vibration isolator. *Physics Letters A*, 374(36):3705–3709, 2010.

[44] M. Scala, M. S. Kim, G. W. Morley, P. F. Barker, and S. Bose. Matter-wave interferometry of a levitated thermal nano-oscillator induced and probed by a spin. *Phys. Rev. Lett.*, 111:180403, Oct 2013.

[45] Fernando C Lombardo and Paula I Villar. Dephasing in matter-wave interferometry. *Journal of Physics A: Mathematical and General*, 39(21):6509, may 2006.

[46] Zhang-qi Yin, Tongcang Li, Xiang Zhang, and L. M. Duan. Large quantum superpositions of a levitated nanodiamond through spin-optomechanical coupling. *Phys. Rev. A*, 88:033614, Sep 2013.

[47] Xing-Yan Chen and Zhang-Qi Yin. High-precision gravimeter based on a nano-mechanical resonator hybrid with an electron spin. *Opt. Express*, 26(24):31577–31588, Nov 2018.

[48] Ryszard Horodecki, Paweł Horodecki, Michał Horodecki, and Karol Horodecki. Quantum entanglement. *Rev. Mod. Phys.*, 81:865–942, Jun 2009.

[49] Martine Schut, Jules Tilly, Ryan J. Marshman, Sougato Bose, and Anupam Mazumdar. Improving resilience of quantum-gravity-induced entanglement of masses to decoherence using three superpositions. *Phys. Rev. A*, 105:032411, Mar 2022.

[50] Jules Tilly, Ryan J. Marshman, Anupam Mazumdar, and Sougato Bose. Qudits for witnessing quantum-gravity-induced entanglement of masses under decoherence. *Phys. Rev. A*, 104:052416, Nov 2021.

[51] Thomas W. van de Kamp, Ryan J. Marshman, Sougato Bose, and Anupam Mazumdar. Quantum gravity witness via entanglement of masses: Casimir screening. *Phys. Rev. A*, 102:062807, Dec 2020.

[52] Pippa Storey and Claude Cohen-Tannoudji. The feynman path integral approach to atomic interferometry: A tutorial. *Journal De Physique Ii*, 4:1999–2027, 1994.

[53] Meng-Zhi Wu. Acceleration Noise Induced Decoherence in Stern-Gerlach Interferometers for Gravity Experiments. 6 2024.

[54] P. Mohazzabi and B.M. Shefchik. A universal relationship between spring constant and torsion constant. *Journal of Physics and Chemistry of Solids*, 62(4):677–681, 2001.

[55] Stephen H. Crandall, Norman C. Dahl, and Ellis Harold Dill. An introduction to the mechanics of solids. 1972.

[56] Quentin Beaufils, Julien Lefebve, Joel Gomes Baptista, Raphaël Piccon, Valentin Cambier, Leonid A. Sidorenkov, Christine Fallet, Thomas Lévèque, Sébastien Merlet, and Franck Pereira Dos Santos. Rotation related systematic effects in a cold atom interferometer onboard a nadir pointing satellite. *npj Microgravity*, 9(1):53, Jul 2023.

[57] Eric Poisson, Adam Pound, and Ian Vega. The motion

of point particles in curved spacetime. *Living Reviews in Relativity*, 14(1):7, Sep 2011.

[58] Weihuan Chen, Shiing-shen Chern, and Kai S Lam. *Lectures on differential geometry*, volume 1. World Scientific Publishing Company, 1999.

[59] Evert Jan Post. Sagnac effect. *Reviews of Modern Physics*, 39(2):475, 1967.

[60] Ronald Anderson, HR Bilger, and GE Stedman. Sagnac effect: A century of earth-rotated interferometers. *American Journal of Physics*, 62(11):975–985, 1994.

[61] Grigorii B Malykin. The sagnac effect: correct and incorrect explanations. *Physics-Uspekhi*, 43(12):1229, 2000.

[62] Marko Toroš, Sara Restuccia, Graham M Gibson, Marion Cromb, Hendrik Ulbricht, Miles Padgett, and Daniele Faccio. Revealing and concealing entanglement with non-inertial motion. *Physical Review A*, 101(4):043837, 2020.

[63] George B Arfken and Hans-Jurgen Weber. Mathematical methods for physicists. 1972.

[64] Don S Lemons and Anthony Gythiel. Paul langevin's 1908 paper" on the theory of brownian motion"[" sur la thiorie du mouvement brownien," cr acad. sci.(paris) 146, 530-533 (1908)]. *American Journal of Physics*, 65:1079–1081, 1997.

[65] A. Cavalleri, G. Ciani, R. Dolesi, A. Heptonstall, M. Hueller, D. Nicolodi, S. Rowan, D. Tombolato, S. Vitale, P. J. Wass, and W. J. Weber. Increased brownian force noise from molecular impacts in a constrained volume. *Phys. Rev. Lett.*, 103:140601, Sep 2009.

[66] A. Cavalleri, G. Ciani, R. Dolesi, M. Hueller, D. Nicolodi, D. Tombolato, S. Vitale, P.J. Wass, and W.J. Weber. Gas damping force noise on a macroscopic test body in an infinite gas reservoir. *Physics Letters A*, 374(34):3365–3369, 2010.

Appendix A: Lagrangian of Inertial Torsion Noise

In this appendix, we will derive the Lagrangian in Eq. (5) that gives rise to inertial torsion noise (ITN). The basic idea is firstly to construct the metric in the comoving reference frame of the experimental apparatus (Sec. A 1), and then to compute the Lagrangian of the test mass in the non-relativistic limit (Sec. A 2).

1. Rotating Fermi Normal Coordinates

To construct the coordinate system near the experiment, one can choose the worldline of the center of the experimental box as a fiducial time-like curve in the spacetime manifold. Based on this worldline, one can construct the Fermi normal coordinate (FNC) of the spacetime using the method of the Fermi-Walker transport. Under this coordinate, the metric can be generally written as [57]

$$ds^2 = -\left[\left(1 + \frac{a^b x'_b}{c^2}\right)^2 + R_{0c0d}x'^c x'^d\right]c^2 dt'^2 - \frac{2}{3}R_{0cbd}x'^c x'^d c\,dt'\,dx^b + \left(\delta_{bc} - \frac{1}{3}R_{bdce}x'^d x'^e\right)dx'^b dx'^c, \qquad (A1)$$

where the indices $a, b, c, d = 1, 2, 3$ represent the spacial coordinates. In the following, we will neglect the linear acceleration terms $\sim a^b$ and the Riemann tensor terms $\sim R_{abcd}$ such that the Metric in Eq. (A1) reduces to the Minkowski spacetime metric in Cartesian coordinates.

To obtain the metric in a rotating reference frame we have to make an additional transformation. Rotations along the z-axis can be described by the time-dependent angle $\theta(t)$, such that the coordinates in the rotating frame are described by

$$\begin{cases} t = t', \\ x = x'\cos\theta(t) + y'\sin\theta(t), \\ y = -x'\sin\theta(t) + y'\cos\theta(t), \\ z = z', \end{cases} \qquad (A2)$$

where we recall the primed symbols represent the coordinates in the inertial (non-rotating) frame (see Fig. 9).

To compute the metric in the rotating coordinates one can proceed is several ways. For example, one way to simplify the calculation is to write the transformation between (x, y) and (x', y'), as well as between (dx, dy) and (dx', dy'), in matrix form. But here, we will offer an alternative method by exploiting the complex notation. The basic idea is to introduce a complex coordinate $w = x + \mathrm{i}y$, then the complex conjugate is $\bar{w} = x - \mathrm{i}y$, and the differentials are

$$dw = dx + \mathrm{i}dy, \qquad d\bar{w} = dx - \mathrm{i}dy, \qquad (A3)$$

with analogous expressions for the primed variables. This is a common trick to deal with 2D problems, because one can always construct a complex structure on a 2D surface through its metric to become a Riemann surface. For pedagogical material, see chapter 7 of [58].
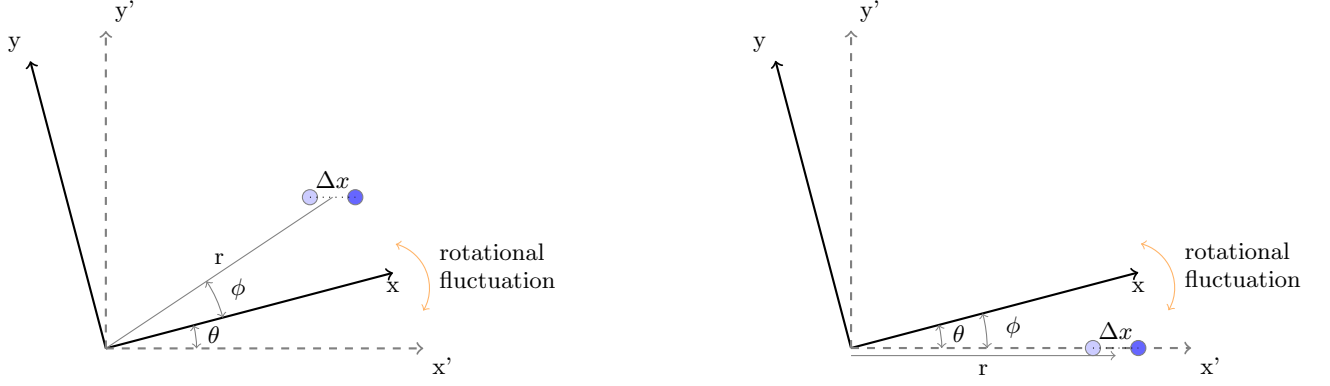
FIG. 9. Illustration of the inertial reference frame (labeled as x' and y') and of the rotating reference frame (labeled as x and y), which is comoving with the experimental equipment. For simplicity, we assume that the interferometric axis (line segment connecting the light and dark blue circles) is aligned with the x' axis of the inertial frame. (a) General case when the interferometric particle is placed at angle $\phi + \theta$ with respect to the inertial reference frame. ϕ denotes its polar coordinate in the rotating reference frame, and θ is the angle between the inertial and rotating reference frames. (b) Special case when the interferometric axis coincides with the x'-axis of the inertial reference frame. In this case, the two angles ϕ and θ defined in point (a) have a simple relationship $\phi = -\theta$.

The rotation transformation from Eq. (A2), as well as its inverse, can be simply written as

$$w = w' e^{i\theta(t)}, \qquad w' = w e^{-i\theta(t)}, \tag{A4}$$

where we have omitted the t and z coordinate transformation for brevity. We find that the differential forms are

$$
\begin{aligned}
dw' &= e^{-i\theta} dw' - i\dot{\theta} w' e^{-i\theta} dt, \\
d\bar{w}' &= e^{i\theta} d\bar{w}' + i\dot{\theta} \bar{w}' e^{i\theta} dt.
\end{aligned}
\tag{A5}
$$

The considered terms $dx'^2 + dy'^2 = dw' d\bar{w}'$ in the original Fermi normal coordinates from Eq. (A1) transform to

$$
\begin{aligned}
dw' d\bar{w}' &= (e^{-i\theta} dw - i\dot{\theta} w e^{-i\theta} dt)(e^{i\theta} d\bar{w} + i\dot{\theta} \bar{w} e^{i\theta} dt) \\
&= dw d\bar{w} - i\dot{\theta}(w d\bar{w} - \bar{w} dw) dt + \dot{\theta}^2 w \bar{w} dt^2 \\
&= dx^2 + dy^2 + 2\dot{\theta}(-x dy + y dx) dt + \dot{\theta}^2 (x^2 + y^2) dt^2,
\end{aligned}
\tag{A6}
$$

which then immediately gives the transformed metric in the rotating reference frame

$$ds^2 = -\big(c^2 - \dot{\theta}^2(x^2 + y^2)\big) dt^2 + 2\dot{\theta}(-x dy + y dx) dt + dx^2 + dy^2. \tag{A7}$$

2. Lagrangian of Inertial Torsion Noise

The Lagrangian of a point-like massive object is given by $L = -mc^2 \sqrt{-ds^2/(c^2 dt^2)}$. Using the metric in Eq. (A7) and taking the non-relativistic limit $v_x, v_y \ll c$ (with $v_x \equiv dx/dt, v_y \equiv dy/dt$), we find that the Lagrangian is

$$L = -\frac{1}{2} m \dot{\theta}^2 (x^2 + y^2) + m\dot{\theta}(-x v_y + v_x y), \tag{A8}$$

where we have omitted the constant term mc^2 and the kinetic energy term $1/2 m(v_x^2 + v_y^2)$. The term $-\frac{1}{2} m \dot{\theta}^2 (x^2 + y^2)$ describes the centrifugal force. In particular, according to Euler-Lagrange equation $\frac{d}{dt}\left(\frac{\partial L}{\partial \dot{x}_j}\right) - \frac{\partial L}{\partial x_j} = 0$, this term gives the centrifugal force $\vec{F}_{\text{cent}} = m\dot{\theta}^2 \vec{r}$. The term $m\dot{\theta}(-x v_y + v_x y)$ will give two forces, $-2m\vec{r} \times \dot{\vec{\theta}}$ and $m\vec{r} \times \ddot{\vec{\theta}}$, known as the Coriolis force and the Euler force, respectively. Eq. (A8) is well known in the literature, and it gives rise among other things also to the Sagnac effect [59–62].
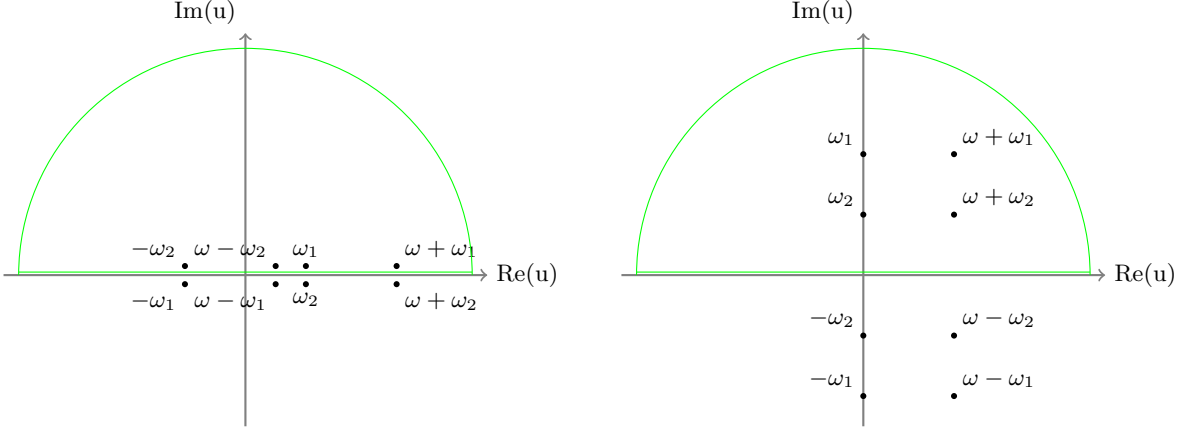
FIG. 10. The poles and the integral path of the integral in Eq. (B1). The poles of $S_{\Theta\Theta}$ and $S_{\dot{\Theta}^2\dot{\Theta}^2}(\omega)$ are given by Eq. (B2). Subfigure (a) and (b) show two cases where $\sqrt{\Omega_{\rm rot}^2 - \gamma_{\rm rot}^2/4}$ is a real number and an imaginary number. Note that the relations $\omega_3 = -\omega_2$ and $\omega_4 = -\omega_1$ have been used to simplify the notation in both subfigures.

The Lagrangian term $m\dot{\theta}(-xv_y + v_x y)$ can be written into polar coordinates with $x = r\cos\phi$ and $y = r\sin\phi$ (see Fig. 9(a)). If r is assumed constant, then $v_x = -r\dot{\phi}\sin\phi$ and $v_y = r\dot{\phi}\cos\phi$, so this term becomes $-mr^2\dot{\theta}\dot{\phi}$. In the special case shown in Fig. 9(b), when the test mass is set on the x-axis of the inertial (non-rotating) reference frame, one may directly obtain $\phi = -\theta$. Then the Lagrangian of the Coriolis and Euler forces becomes $m\dot{\theta}^2 r^2$. Therefore, the total Lagrangian of the centrifugal, the Coriolis, and the Euler forces reduces to

$$L_{\rm ITN} = \frac{1}{2}m\dot{\theta}^2 r^2. \tag{A9}$$

Finally, if the angle θ is assumed to be small, then the y-component is much smaller than the x-component in the Lagrangian. Hence making the approximation $r \approx x$ we finally obtain the ITN Lagrangian in Eq. (5).

Appendix B: Calculation for PSD of ITN

In this appendix, we will calculate the PSD of the ITN arising from a thermal environment modelled by Eq. (C1). As is discussed in the main text, the PSD of ITN $S_{\dot{\Theta}^2\dot{\Theta}^2}(\omega)$ is the self-convolution of the PSD of the torsion angle $S_{\dot{\Theta}\dot{\Theta}}(\omega) = \omega^2 S_{\Theta\Theta}(\omega)$, that is,

$$
\begin{aligned}
S_{\dot{\Theta}^2\dot{\Theta}^2}(\omega) &= (S_{\dot{\Theta}\dot{\Theta}} * S_{\dot{\Theta}\dot{\Theta}})(\omega) \\
&= \int_{-\infty}^{\infty} (2\gamma_{\rm rot}k_B T/I)^2 \frac{u^2}{(u^2 - \Omega_{\rm rot}^2)^2 + \gamma_{\rm rot}^2 u^2} \times \frac{(\omega - u)^2}{((\omega - u)^2 - \Omega_{\rm rot}^2)^2 + \gamma_{\rm rot}^2(\omega - u)^2} {\rm d}u.
\end{aligned} \tag{B1}
$$

We will use the residue theorem to calculate this integral [63]. Firstly, the poles of $S_{\Theta\Theta}(\omega)$ are

$$\omega_{1,2,3,4} = \pm\sqrt{\Omega_{\rm rot}^2 - \gamma_{\rm rot}^2/4} \pm i\gamma_{\rm rot}/2. \tag{B2}$$

The positiveness of the discriminant $\Omega_{\rm rot}^2 - \gamma_{\rm rot}^2/4$ will affect the positions of poles of the integrand in Eq. (B1), shown in Fig. 10, of which the discriminants in sub-figures (a) and (b) are positive and negative respectively. Note that the relations $\omega_3 = -\omega_2$ and $\omega_4 = -\omega_1$ are used to simplify the notations in both sub-figures. However, since the integral is real-valued, both cases should have the same result. Thus, it is enough to consider the case $\Omega_{\rm rot}^2 - \gamma_{\rm rot}^2/4 > 0$.

Then according to the residue theorem, the integral value in Eq. (B1) equals the residue value of the integrand at the poles in the path shown in Fig. 10. In particular, this integral equals the summation of the residues at ω_1, $-\omega_2$, $\omega + \omega_1$ and $\omega - \omega_2$ when $\omega \neq \omega_1 + \omega_2$. In this case, every pole is a first-order pole. For the special case $\omega = \omega_1 + \omega_2$, there are only two second-order poles ω_1 and ω_2, so the integral in Eq. (B1) is given by these two poles. Since our purpose is to calculate the pure real-valued integral (B1) and different cases of poles have to give the same result, we may focus on the case $\omega \neq \omega_1 + \omega_2 = 2\sqrt{\Omega_{\rm rot}^2 - \gamma_{\rm rot}^2/4}$, then the integrand can be written as

$$F(u,\omega) = A^2 \frac{u^2(\omega-u)^2}{(u-\omega_1)(u-\omega_2)(u+\omega_1)(u+\omega_2)} \times \frac{1}{(u-(\omega-\omega_1))(u-(\omega-\omega_2))(u-(\omega+\omega_1))(u-(\omega+\omega_2))}, \quad \text{(B3)}$$

where we denote $A = 2\gamma_{\rm rot}k_BT/I$ for ease of writing. Then the residue values are given by

$$
\begin{aligned}
2\pi\mathrm{i}\operatorname*{Res}_{u=\omega_1} F(u) &= A^2 \frac{\pi\omega_1(\omega-\omega_1)^2}{2\gamma_{\rm rot}\sqrt{\Omega_{\rm rot}^2-\gamma_{\rm rot}^2/4}} \times \frac{1}{\omega(\omega-\mathrm{i}\gamma_{\rm rot})(\omega-2\sqrt{\Omega_{\rm rot}^2-\gamma_{\rm rot}^2/4})(\omega-2\omega_1)}, \\
2\pi\mathrm{i}\operatorname*{Res}_{u=-\omega_2} F(u) &= A^2 \frac{\pi\omega_2(\omega+\omega_2)^2}{2\gamma_{\rm rot}\sqrt{\Omega_{\rm rot}^2-\gamma_{\rm rot}^2/4}} \times \frac{1}{\omega(\omega-\mathrm{i}\gamma_{\rm rot})(\omega+2\sqrt{\Omega_{\rm rot}^2-\gamma_{\rm rot}^2/4})(\omega+2\omega_2)}, \\
2\pi\mathrm{i}\operatorname*{Res}_{u=\omega+\omega_1} F(u) &= A^2 \frac{(\omega+\omega_1)^2\omega_1^2}{\omega(\omega+\mathrm{i}\gamma_{\rm rot})(\omega+2\omega_1)(\omega+2\sqrt{\Omega_{\rm rot}^2-\gamma_{\rm rot}^2/4})} \times \frac{\pi}{2\omega_1\gamma_{\rm rot}\sqrt{\Omega_{\rm rot}^2-\gamma_{\rm rot}^2/4}}, \\
2\pi\mathrm{i}\operatorname*{Res}_{u=\omega-\omega_2} F(u) &= A^2 \frac{(\omega-\omega_2)^2\omega_2^2}{\omega(\omega-2\sqrt{\Omega_{\rm rot}^2-\gamma_{\rm rot}^2/4})(\omega-2\omega_2)(\omega+\mathrm{i}\gamma_{\rm rot})} \times \frac{\pi}{2\omega_2\gamma_{\rm rot}\sqrt{\Omega_{\rm rot}^2-\gamma_{\rm rot}^2/4}}.
\end{aligned}
\quad \text{(B4)}
$$

Finally the PSD of ITN defined as the integral (B1) is

$$
\begin{aligned}
S_{\dot{\Theta}^2\dot{\Theta}^2}(\omega) &= 2\pi\mathrm{i}(\operatorname*{Res}_{u=\omega_1} F(u) + \operatorname*{Res}_{u=-\omega_2} F(u) + \operatorname*{Res}_{u=\omega+\omega_1} F(u) + \operatorname*{Res}_{u=\omega-\omega_2} F(u)) \\
&= A^2 \frac{\pi}{\gamma_{\rm rot}} \frac{4\omega^4 + 4(\gamma_{\rm rot}^2 - 3\Omega_{\rm rot}^2)\omega^2 + 16\Omega_{\rm rot}^4}{(\omega^2+\gamma_{\rm rot}^2)(4\gamma_{\rm rot}^2\omega^2+(\omega^2-4\Omega_{\rm rot}^2)^2)}.
\end{aligned}
\quad \text{(B5)}
$$

Appendix C: Gas collision noise

In this appendix, we will consider a certain source of the inertial torsion noise, that is, the collision due to thermal motion of gas molecules. According to the fluctuation-dissipation theorem, the applitute of the random force due to the gas collision is $\sqrt{A} = \sqrt{2\gamma_{\rm rot}k_BT/I}$, where k_B is the Boltzmann constant and $T = 300\,\mathrm{K}$ is the gas temperature outside the experiment box. Then the dynamical equation (17) of the torsion motion of the experiment box becomes to the Langevin equation [64]

$$\ddot{\Theta} = -\Omega_{\rm rot}^2\Theta - \gamma_{\rm rot}\dot{\Theta} + \sqrt{2\gamma_{\rm rot}k_BT/I}\,\Theta_{\rm in}, \quad \text{(C1)}$$

In this case, the power spectrum for Θ and $\dot{\Theta}^2$ are

$$
\begin{aligned}
S_{\Theta\Theta}(\omega) &= \frac{2\gamma_{\rm rot}k_BT/I}{(\Omega_{\rm rot}^2-\omega^2)^2 + \gamma_{\rm rot}^2\omega^2}, \\
S_{\dot{\Theta}^2\dot{\Theta}^2}(\omega) &= \frac{4\pi\gamma_{\rm rot}(k_BT)^2}{I^2} \frac{4\omega^4 + 4(\gamma_{\rm rot}^2 - 3\Omega_{\rm rot}^2)\omega^2 + 16\Omega_{\rm rot}^4}{(\omega^2+\gamma_{\rm rot}^2)(4\gamma_{\rm rot}^2\omega^2+(\omega^2-4\Omega_{\rm rot}^2)^2)}.
\end{aligned}
\quad \text{(C2)}
$$

It is notatble that $S_{\dot{\Theta}^2\dot{\Theta}^2}(\omega)$ has an additional γ^2 dependence in comparison to the general case in Eq. (20). This difference arises because the amplitude $A = 2\gamma_{\rm rot}k_BT/I$ of the external force for the thermal noise in Eq. (C1) is proportional to the damping rate $\gamma_{\rm rot}$, which does not hold for the general case considered in this section.

Note that in this case, the damping rate $\gamma_{\rm rot}$ describes both the dissipation effect and the random force caused by the collision from the ambient thermal gas molecules, which is given by [65, 66]

$$\gamma_{\rm rot} = \frac{L^4}{I}\left(1 + \frac{\pi}{12}\right) P_{\rm gas} \sqrt{\frac{2m_{\rm gas}}{\pi k_BT}}, \quad \text{(C3)}$$

where $P_{\rm gas}$ is the pressure of gas and $m_{\rm gas}$ is the mass of the gas molecules. Since $\gamma_{\rm rot}$ is proportional to $P_{\rm gas}$, it can vary depending on the gas pressure outside the box. Apart from $P_{\rm gas}$, all other factors contribute a factor around $10^{-4} \sim 10^{-3}\,\mathrm{Hz/Pa}$, so the value of the damping rate $\gamma_{\rm rot}$ can be estimated as

$$\gamma_{\rm rot}/[\mathrm{Hz}] \sim 10^{-4}P_{\rm gas}/[\mathrm{Pa}]. \quad \text{(C4)}$$
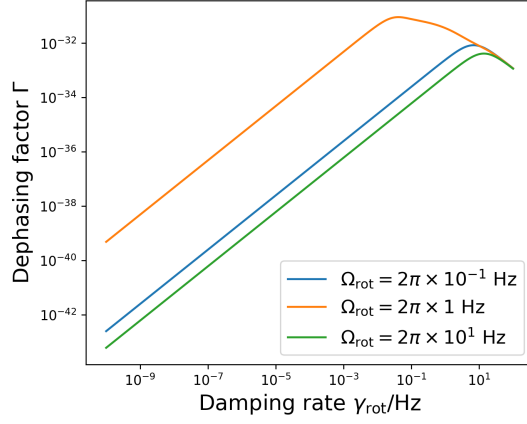
FIG. 11. Dephasing factor Γ as a function of the damping factor γ_{rot} for the thermal case. The transfer function is given in Eq. (11) with parameters $t_a = 0.25\,\mathrm{s}$ and $t_e = 0\,\mathrm{s}$. Three different Ω_{rot} are chosen in the low rotation frequency limit (blue line), the resonance frequency condition $\Omega_{\mathrm{rot}} \sim 2\pi/T = 2\pi\,\mathrm{Hz}$ (orange line), and the high rotation frequency limit (green line). The dephasing Γ is proportional to γ_{rot} when $\gamma_{\mathrm{rot}} \ll \Omega_{\mathrm{rot}}$, while it starts decreasing with respect to γ_{rot} when γ_{rot} becomes comparable or larger than Ω_{rot}.

For instance, in the atmosphere pressure $P_{\mathrm{gas}} = 10^5\,\mathrm{Pa}$, the damping rate is $\gamma_{\mathrm{rot}} \sim 10^1\,\mathrm{Hz}$. When the gas pressure outside the experiment box is pumped as $10^2\,\mathrm{Pa}$ or $10^{-6}\,\mathrm{Pa}$ by a rough-vacuum pump or a series of ultra-high-vacuum pumps respectively, the corresponding damping rates γ_{rot} are $10^{-2}\,\mathrm{Hz}$ and $10^{-10}\,\mathrm{Hz}$ for respect. Note that a value $\gamma_{\mathrm{rot}} \sim 10^{-9}\,\mathrm{Hz}$ has already been measured in experiment [65].

As for the dephasing factor, Fig. 11 shows the dependence of Γ on the damping factor γ_{rot} caused by the thermal gas molecules. As is shown, for the thermal case, Γ is proportional to γ_{rot} and $\gamma_{\mathrm{rot}}^{-1}$ in the underdamped region and the overdamped region in respect, which has an additional γ^2 dependence in comparison to the general case because the thermal amplitude A^2 is proportional to γ_{rot}^2.

A final remark on Fig.11 is that the dephasing factor Γ caused by the torsion noise from gas molecules collision is negligibly tiny. Two main reasons cause this. First, the thermal motion of gas molecules is proportional to a small thermal factor $k_B T \sim 10^{-21}\,\mathrm{J}$. Besides, ITN is a second-order effect, so every little factor in the PSD $S_{\Theta\Theta}(\omega)$ of the experiment apparatus will be squared for the dephasing factor Γ. Combining both effects, the dephasing factor Γ is suppressed by a highly tiny factor $(k_B T)^2 \sim 10^{-42}\,\mathrm{J}^2$, such that Γ does not exceed 10^{-30}.